AIAA JOURNAL
Vol. 37, No. 3, March 1999

Multidomain Spectral Computations of Sound Radiation from Ducted Fans

D. Stanescu*
Concordia University, Montreal, Quebec H3G 1M8, Canada
D. Ait-Ali-Yahia†
Pratt and Whitney Canada, United Technologies Corporation, Longueuil, Quebec J4G 1A1, Canada
W. G. Habashi‡
Concordia University, Montreal, Quebec H3G 1M8, Canada
and
M. P. Robichaud§
Pratt and Whitney Canada, United Technologies Corporation, Longueuil, Quebec J4G 1A1, Canada

A time-domain method for acoustic propagation and its application to tone noise radiated from rigid-wall fan inlets are presented. The noise propagation phenomena are modeled by the nonlinear time-dependent Euler equations written in conservative form. The equations are solved numerically using a staggered-grid multidomain Chebyshev discretization for the spatial terms and a Runge–Kutta scheme for time integration. Various types of radiation boundary conditions are implemented and investigated on generic benchmarks. The resulting code is optimized on parallel machines with shared memory. The method is first validated on noise radiation from two-dimensional and axisymmetric flat ducts with no mean flow for which analytical data exist. The full potential of the method is then tested by computing the sound field radiated from an axisymmetric bell-mouth duct in a nonuniform mean flow. Three-dimensional computations of the sound field in a bent pipe, on which both experiments and computations using a boundary integral method have been carried out at ONERA, are also presented.

Introduction

BUILDING modern turbofan engines with higher bypass ratios is significantly limited by increasingly restrictive airport noise standards. For approach and takeoff, the fan rotor–stator interactions and leading-edge shocks become the primary sources of noise as the bypass ratio is increased above a certain threshold. The acoustic field of such phenomena is characterized by high levels of acoustic pressure and nonuniform mean flows so that numerical analyses based on linear models are inadequate and may lead to inaccurate predictions.

These limitations drove some researchers[1,2] to consider the nonlinear Euler/Navier–Stokes equations for fan inlet sound radiation modeling. This approach, while removing the heavy assumptions under which fan noise is usually predicted nowadays, faces its intrinsic difficulties. A most important one is to ensure proper radiation boundary conditions that remain valid for nonuniform mean flows. Also, the discretization must allow propagation of waveforms over large distances with minimal phase and amplitude errors. However, the most important challenge is to minimize these errors with reasonable numbers of points per wavelength while satisfying the dispersion relation of the governing equations[3]; otherwise computer resources may soon become prohibitive with increasing frequencies.

Spectral methods seem a natural choice for wave propagation due to their low dispersion and dissipation properties. In particular, when three spatial directions are involved, their low requirement in number of points per wavelength (typically 2 or π points per wavelength for Fourier or Chebyshev approximation,[4] respectively) allows time-domain simulation of high-frequency aeroacoustic phenomena with reasonable computer memory and CPU time. The use of spectral methods was usually restricted to simple geometries and, in the Fourier case, to periodic boundary conditions. Multidomain and spectral element methods[5–7] emerged relatively recently to increase the geometric flexibility of the method. When convection is present, one particular difficulty in this case is ensuring the proper direction of signal propagation at element/domain interfaces. Among the approaches proposed to this end, the staggered-grid method[7] offers the advantage that domain corners are not included in the approximation. Proper upwinding can be ensured as in finite volume solvers by the use of flux-vector/flux-difference splitting.

The present paper presents applications of the staggered-grid multidomain spectral method to computations of tonal noise radiation from ducts with rigid walls. The system of full nonlinear time-dependent Euler equations is used to model both the mean flow and the acoustic field. Acoustic variables are obtained by subtracting the mean flow from the time-dependent variables. Several types of radiation boundary conditions are tested at open field boundaries, and various incoming duct acoustic modes are considered at the source plane.

The method is first validated on linear cases to demonstrate its ability to handle a linear subset of the governing equations. This is done by comparing computed far-field directivity patterns with analytical results for slab symmetry and axisymmetric flat ducts. Axisymmetric propagation of high-level acoustic perturbations in a nonuniform mean flow and the performance of the radiation boundary conditions are then explored on a bell-mouth fan inlet.

In the present time-domain approach, modeling higher-order spinning modes that characterize fan noise requires a three-dimensional framework. Therefore, a test of the three-dimensional version of the code is also performed on the acoustic propagation of both plane waves and spinning modes in a generic model of a turboshaft helicopter engine inlet, a problem that was investigated both

Presented as Paper 98-2266 at the AIAA/CEAS 4th Aeroacoustics Conference, Toulouse, France, June 2–4, 1998; received July 22, 1998; revision received Nov. 24, 1998; accepted for publication Dec. 4, 1998.

*Ph.D. Candidate, Computational Fluid Dynamics Laboratory, Department of Mechanical Engineering, 1455 de Maisonneuve Boulevard West. E-mail: dan@cfdlab.concordia.ca. Student Member AIAA.

†Senior Research Engineer, Analytical Systems, 1000 Marie-Victorin (01SA4). Member AIAA.

‡Professor and Director, Computational Fluid Dynamics Laboratory, Department of Mechanical Engineering, 1455 de Maisonneuve Boulevard West. Associate Fellow AIAA.

§Computational Fluid Dynamics Group Leader, Analytical Systems, 1000 Marie-Victorin (01SA4). Member AIAA.

experimentally and numerically, using a boundary integral method, by Malbéqui et al.[8] at ONERA.

Governing Equations and Discretization

The system of Euler equations is written here as

$$\frac{\partial \boldsymbol{Q}}{\partial t} + \sum_{i=1}^{m} \frac{\partial \boldsymbol{F}_i}{\partial x_i} + \nu \boldsymbol{H} \delta_{m2} = 0 \tag{1}$$

where m is the number of spatial dimensions and $\nu = 0$ or $\nu = 1$ for slab and axial symmetry (in which case x_2 is the radial coordinate), respectively. The state vector $\boldsymbol{Q}$ and the flux vectors $\boldsymbol{F}_i$ are given by

$$\boldsymbol{Q} = \begin{bmatrix} \rho \\ \rho v_1 \\ \rho v_2 \\ \rho v_3 \\ \rho E \end{bmatrix}, \qquad \boldsymbol{F}_i = \begin{bmatrix} \rho v_i \\ \rho v_1 v_i + p\delta_{1i} \\ \rho v_2 v_i + p\delta_{2i} \\ \rho v_3 v_i + p\delta_{3i} \\ (\rho E + p) v_i \end{bmatrix} \tag{2}$$

and the source term $\boldsymbol{H}$ has the form

$$\boldsymbol{H} = \frac{1}{x_2} \begin{bmatrix} \rho v_2 \\ \rho v_1 v_2 \\ \rho v_2^2 \\ (\rho E + p) v_2 \end{bmatrix} \tag{3}$$

The computational domain is divided into nonoverlapping quadrilateral (two-dimensional) or hexahedral (three-dimensional) elements that are transformed under an isoparametric mapping $\xi_i(x_1, \ldots, x_m)$ obtained through transfinite interpolation on the master element $\Omega_M = [-1, 1]^m$. To avoid confusion, the word *element* is used here to describe any region on which a stand-alone spectral approximation is performed. Under this mapping, Eq. (1) becomes

$$\frac{\partial \tilde{\boldsymbol{Q}}}{\partial t} + \sum_{i=1}^{m} \frac{\partial \tilde{\boldsymbol{F}}_i}{\partial \xi_i} + \nu \boldsymbol{H} \delta_{m2} = 0 \tag{4}$$

where the transformed components of the state and flux vectors are obtained using the Jacobian of the transformation J and the components of the metric tensor:

$$\tilde{\boldsymbol{Q}} = \frac{\boldsymbol{Q}}{J}, \qquad \tilde{F}_i = \frac{1}{J} \sum_{k=1}^{m} \frac{\partial \xi_i}{\partial x_k} \boldsymbol{F}_k$$
$$J = \det\left[\frac{\partial(\xi_1, \ldots, \xi_m)}{\partial(x_1, \ldots, x_m)} \right] \tag{5}$$

Let the sets G and L denote the Gauss–Chebyshev and the Gauss–Chebyshev–Lobatto points, respectively:

$$G = \left\{ \bar{\xi}^j \mid \bar{\xi}^j = -\cos\left[\frac{(2j-1)\pi}{2N} \right], \quad j = \overline{1, N} \right\} \tag{6}$$

$$L = \left\{ \xi^j \mid \xi^j = -\cos\left(\frac{j\pi}{N} \right), \quad j = \overline{0, N} \right\} \tag{7}$$

where N is the maximum polynomial order present in the approximation. The state vector $\tilde{\boldsymbol{Q}}$ and the source vector $\boldsymbol{H}$ are collocated at the set of points G^m, the tensor product of the one-dimensional sets of Gauss–Chebyshev points. The flux components are, on the other hand, collocated on grids obtained by replacing the Gauss–Chebyshev points with the Lobatto points for the corresponding flux direction in the preceding tensor product; for example, $\tilde{\boldsymbol{F}}_1$ is collocated at $L \times G^{m-1}$ and $\tilde{\boldsymbol{F}}_3$ at $G^{m-1} \times L$.

To solve the system (1) under a semidiscrete formulation, the spatial operator is first approximated. At the beginning of a time step, the initial data are the state vector values $\tilde{\boldsymbol{Q}}$ at the points G^m. From these values one can create a multidimensional interpolant of the form

$$\tilde{\boldsymbol{Q}}(\xi_1, \xi_2, \xi_3) = \sum_{G^m} \tilde{\boldsymbol{Q}}\left(\bar{\xi}_1^i, \bar{\xi}_2^j, \bar{\xi}_3^k\right) \bar{h}_i(\xi_1) \bar{h}_j(\xi_2) \bar{h}_k(\xi_3) \tag{8}$$

where the interpolating Lagrange polynomials $\bar{h}(\xi)$ corresponding to the set of Gauss–Chebyshev points G,

$$\bar{h}_i(\xi) = \prod_{l=1, l \neq i}^{N} \left(\frac{\xi - \bar{\xi}^l}{\bar{\xi}^i - \bar{\xi}^l} \right) \tag{9}$$

have been introduced. From this interpolant the values of the state vector at the flux collocation points can be readily obtained. For example, at the points where the $\tilde{\boldsymbol{F}}_1$ flux is needed, $\tilde{\boldsymbol{Q}}$ can be computed as

$$\tilde{\boldsymbol{Q}}\left(\xi_1^l, \bar{\xi}_2^j, \bar{\xi}_3^k\right) = \sum_{G^m} \tilde{\boldsymbol{Q}}\left(\bar{\xi}_1^i, \bar{\xi}_2^j, \bar{\xi}_3^k\right) \bar{h}_i\left(\xi_1^l\right) \bar{h}_j\left(\bar{\xi}_2^j\right) \bar{h}_k\left(\bar{\xi}_3^k\right) \tag{10}$$

which is in fact a one-dimensional interpolation because $\bar{h}_i(\bar{\xi}^i) = 1$.

At element interfaces there will be two values for the state vector, from the two neighboring elements. To create a continuous flux, a Riemann problem is solved at each interface, with the initial data being the two distinct states. The solution of this problem is then assigned to both neighboring elements. Having the solution at the flux collocation points, one can compute the fluxes. The final step is to compute the flux derivatives at solution collocation points. This is accomplished by writing the transformed flux as

$$\tilde{\boldsymbol{F}}_1(\xi_1, \xi_2, \xi_3) = \sum_{L \times G^{m-1}} \tilde{\boldsymbol{F}}_1\left(\bar{\xi}_1^i, \bar{\xi}_2^j, \bar{\xi}_3^k\right) h_i(\xi_1) \bar{h}_j(\xi_2) \bar{h}_k(\xi_3) \tag{11}$$

where $h(\xi)$ is the Lagrange interpolant based on the Lobatto set of points, L. The needed differential is, therefore,

$$\frac{\partial \tilde{\boldsymbol{F}}_1}{\partial \xi_1}\left(\bar{\xi}_1^i, \bar{\xi}_2^j, \bar{\xi}_3^k\right) = \sum_{L \times G^{m-1}} \tilde{\boldsymbol{F}}_1\left(\xi_1^i, \bar{\xi}_2^j, \bar{\xi}_3^k\right) \frac{\partial h_i}{\partial \xi_1}\left(\bar{\xi}_1^i\right) \bar{h}_j\left(\bar{\xi}_2^j\right) \bar{h}_k\left(\bar{\xi}_3^k\right) \tag{12}$$

Because the number of Gauss–Chebyshev points used in practice is relatively small (up to 20), both interpolation and differentiation are implemented as matrix–vector multiplications. Note that the differentiation in Eq. (12) also represents a one-dimensional operation, which makes the method efficient even for multidimensional flows.

Having obtained an approximation to the spatial terms of Eq. (1), the time integration is performed using an explicit Runge–Kutta scheme. The classical fourth-order scheme and a $4N$-storage version, valid for nonlinear systems, of the low-dissipation and dispersion schemes of Hu et al.[9] are implemented in the two-dimensional code, whereas the $2N$-storage version of Hu's schemes[10] and the fourth-order scheme of Carpenter and Kennedy[11] are used in the three-dimensional version of the code. The reader is referred to Kopriva and Kolias[7] for an exhaustive description of the method in a two-dimensional setting.

Boundary Conditions

This section is limited to the discussion of boundary conditions for acoustic computations. For proper ways of implementing boundary conditions when computing steady states, i.e., mean flows, with the Euler equations, see Ref. 12.

For the far-field boundaries, several types of nonreflecting treatments were investigated. The radiation boundary condition devised by Tam and Webb,[3]

$$\left(\frac{1}{V(\theta)} \frac{\partial}{\partial t} + \frac{\partial}{\partial r} + \frac{1}{\kappa r} \right) \begin{bmatrix} \rho - \bar{\rho} \\ v_1 - \bar{v}_1 \\ v_2 - \bar{v}_2 \\ p - \bar{p} \end{bmatrix} = 0 \tag{13}$$

was first implemented in the $m = 2$ version of the code. This boundary condition is obtained for the case of a uniform mean flow aligned with the x_1 axis, with velocity components $(\bar{v}_1, \bar{v}_2) = (U_0, 0)$. In Eq. (13), r and θ are polar coordinates with respect to the source, the overbar denotes mean flow values, and the group velocity, $V(\theta) = U_0 \cos\theta + \bar{c}(1 - M^2 \sin^2\theta)^{1/2}$, reduces to $\bar{c}$ in no-mean-flow cases. Furthermore, $\kappa = 2$ for slab symmetry and $\kappa = 1$ for axisymmetric cases. To ensure proper upwinding, the boundary fluxes were computed using the Riemann solution between the boundary values given by Eq. (13) and the state interpolated from the interior.

However, this boundary treatment became unstable in some cases involving long time integration if no dissipative mechanism was added. This numerical instability is created mainly by the discontinuities at domain interfaces, which finally show up in the boundary time derivatives. The scheme, however, could be stabilized using an eighth-order sharpened raised cosine filter to smooth the data in the layer of elements next to the boundary before computing the spatial derivatives in Eq. (13).

Using the same information about the source position, the finite wave model developed by Atkins and Casper[13] can be easily accommodated in the multidomain spectral framework. The only modification required is to solve the Riemann problem projected on the ray path from the source instead of on the grid normals, for points lying on the radiation boundary. An isentropic wave assumption allows for an exact, inexpensive solution.[13] This method leads to very good results for the present field solver and at the same time accounts for nonlinear effects and remains valid for nonuniform mean flows. It has been used to obtain all of the results to be presented, unless otherwise noted.

Although the directivity patterns thus obtained could be considered quite satisfactory, a further reduction of the reflections from the boundaries was achieved with the use of an absorbing layer. Similar to the perfectly matched layer techniques[14] but without splitting the equations, such an absorbing layer serves to temporally damp the waves at radiation boundaries. To this end, the governing equations are modified following Freund[15] to

$$\frac{\partial \boldsymbol{Q}}{\partial t} + \sum_{i=1}^{m} \frac{\partial \boldsymbol{F}_i}{\partial x_i} + \nu \boldsymbol{H} \delta_{m2} = -\sigma(\boldsymbol{x})(\boldsymbol{Q} - \bar{\boldsymbol{Q}}) \tag{14}$$

in the layer of boundary elements. The positive value of σ was made to vary from zero to σ_M according to a power law:

$$\sigma(\boldsymbol{x}) = \sigma_M \sum_i \left(\frac{x_i - x_i^{\text{int}}}{x_i^{\text{ext}} - x_i^{\text{int}}} \right)^{\beta} \tag{15}$$

within these elements. (x_i^{int} and x_i^{ext} are the coordinates of the interior and exterior limits of the absorbing layer, limits that lie along planes on which one coordinate is constant.)

Solid wall boundaries are handled by imposing zero normal velocity at the wall using an image-cell method.[7] At the source plane a general function of time and space can be specified for the acoustic perturbation in the present time-domain approach. However, in this work a single duct acoustic mode was specified at the source plane. For the case without mean flow, this is done by solving a Riemann problem with flow variables extrapolated from the interior on one side of the interface and the mean state perturbed with the incoming acoustic mode on the other side. Considering, for example, that the source plane is an annulus of external radius R_0, an incoming spinning mode with azimuthal order s and radial order d, usually denoted by (s, d), is specified by imposing

$$\begin{bmatrix} p - \bar{p} \\ \rho - \bar{\rho} \\ v_x - \bar{v}_x \\ v_r - \bar{v}_r \\ v_\theta - \bar{v}_\theta \end{bmatrix} = A \begin{bmatrix} E_s(k_{sd} r)\cos(k_x x + s\theta - \omega t) \\ (1/\bar{c}^2) E_s(k_{sd} r)\cos(k_x x + s\theta - \omega t) \\ (k_x/\omega\bar{\rho}) E_s(k_{sd} r)\cos(k_x x + s\theta - \omega t) \\ (k_{sd}/\omega\bar{\rho}) E_s'(k_{sd} r)\sin(k_x x + s\theta - \omega t) \\ (s/r\omega) E_s(k_{sd} r)\cos(k_x x + s\theta - \omega t) \end{bmatrix} \tag{16}$$

on the exterior side of the Riemann solver. In this equation, r is the radius nondimensionalized by R_0 and $E_s(k_{sd} r) = J_s(k_{sd} r) + q Y_s(k_{sd} r)$ is the duct eigenfunction, with J_s and Y_s the Bessel functions of first and second kind, respectively. The waviness of the Bessel functions, k_{sd}, and the factor q are determined by the boundary conditions at the casing and hub, with $q = 0$ when there is no centerbody. The axial wave number is $k_x = \sqrt{[(\omega/c)^2 - k_{sd}^2]}$. For nonuniform flow cases, the source plane is treated as a subsonic outlet boundary where only the pressure is imposed as in Eq. (16), whereas the other variables are computed using the solution from inside the computational domain.

Obviously the solution of the Riemann problem does not ensure that waves propagating from the interior of the computational domain toward the source plane do not reflect back in the case when these waves are not plane waves at normal incidence. The present treatment, however, proved satisfactory for all of the cases where a comparison against analytical solutions was carried out. Different ways of treating the source plane as a nonreflecting surface are currently under study.

Results and Discussion

All results that follow are presented in nondimensional form. The reference quantities are ρ_∞ for the density, c_∞ for the velocity components, $\rho_\infty c_\infty^2$ for pressure, and a characteristic length L_c that is specified in each case for distances. Roe's Riemann solver[16] was used at element interfaces.

Flat Ducts

Using the two-dimensional implementation of the method, simulations of noise radiation are performed for both slab- and axisymmetric flat ducts with no mean flow. Results for slab symmetry are presented for the same cases treated by Dong et al.,[17] namely, a nondimensional frequency, $\omega = 15$, with L_c being the duct cross dimension. The amplitude of the incoming waves is 10^{-4}. The computational domain is subdivided into 88 quadrilateral elements of size 1×1, with 13 Gauss–Chebyshev points within each element. This domain discretization gives an average of 5.4 points per wavelength, with a total of 14,872 points within the domain.

Figure 1a shows the computational domain and the Gauss–Chebyshev points grids for the elements inside the duct. To achieve a periodic flowfield, the solution has been marched for 2000 time steps with a four-stage Runge–Kutta scheme. This required 13 min on one R10000 CPU with 195-MHz clock speed of a Silicon Graphics Origin 2000 machine, which gives 24 μs per grid point per time step. Figures 1b–1d display directivity patterns for the plane wave and the first two cross modes, compared to the analytical solutions by Mani.[18] The directivity is obtained by normalizing $\bar{P} \times r^{1/2}$ such that the peak level is at 100 dB, where $\bar{P}$ is the rms pressure on the boundary of the computational domain. As can be seen, the agreement is very good, although some small reflections can be observed at the left-hand-side corners of the domain. Figure 2 presents an instance of the acoustic pressure for the second cross mode.

Directivity results obtained for the same mode with the Tam and Webb[3] radiation boundary condition, Eq. (13), are compared with those obtained using the finite wave model in Fig. 3. As can be seen, the former method leads to higher reflections. This same behavior was actually noticed in all cases that have been computed. To demonstrate the efficiency of the absorbing layer, directivity patterns for the first cross mode calculated with (damping parameters: $\sigma_M = 2.5$ and $\beta = 1$) and without damping are compared in Fig. 4. Practically no more reflections from the boundaries can be noticed, and the agreement with the exact solution becomes excellent. The effect of the absorption can be seen better in Fig. 5, where contour plots of the rms pressure are drawn using the data at Gauss–Chebyshev points. (Note that these data are discontinuous between elements.)

For the axisymmetric case, we do not have the analytical solution that takes into account the presence of the duct walls, although such solutions exist, for example, as given by Savkar.[19] The results for radiation of the first radial mode from a flat circular duct in quiescent fluid are instead compared in Fig. 6 with analytical results for a circular piston vibrating in the same mode[20] ($\bar{P} \times r$, normalized to peak at 100 dB). Because the analytical results do not account for the solid walls, agreement is expected to be less perfect for high values of θ. In this test case, the duct radius is taken as the reference length, and the nondimensional frequency is $\omega = 10.3$. The computational domain extends 14 radii from the duct exit in the axial direction and 11 radii from the axis in the radial direction and is made up of 162 elements on which 10 Gauss–Chebyshev points have been used.

Bell Mouth in Subsonic Flow

The full capabilities of the method are tested on an axisymmetric fan model encased in a bell-mouth duct with a casing thickness of

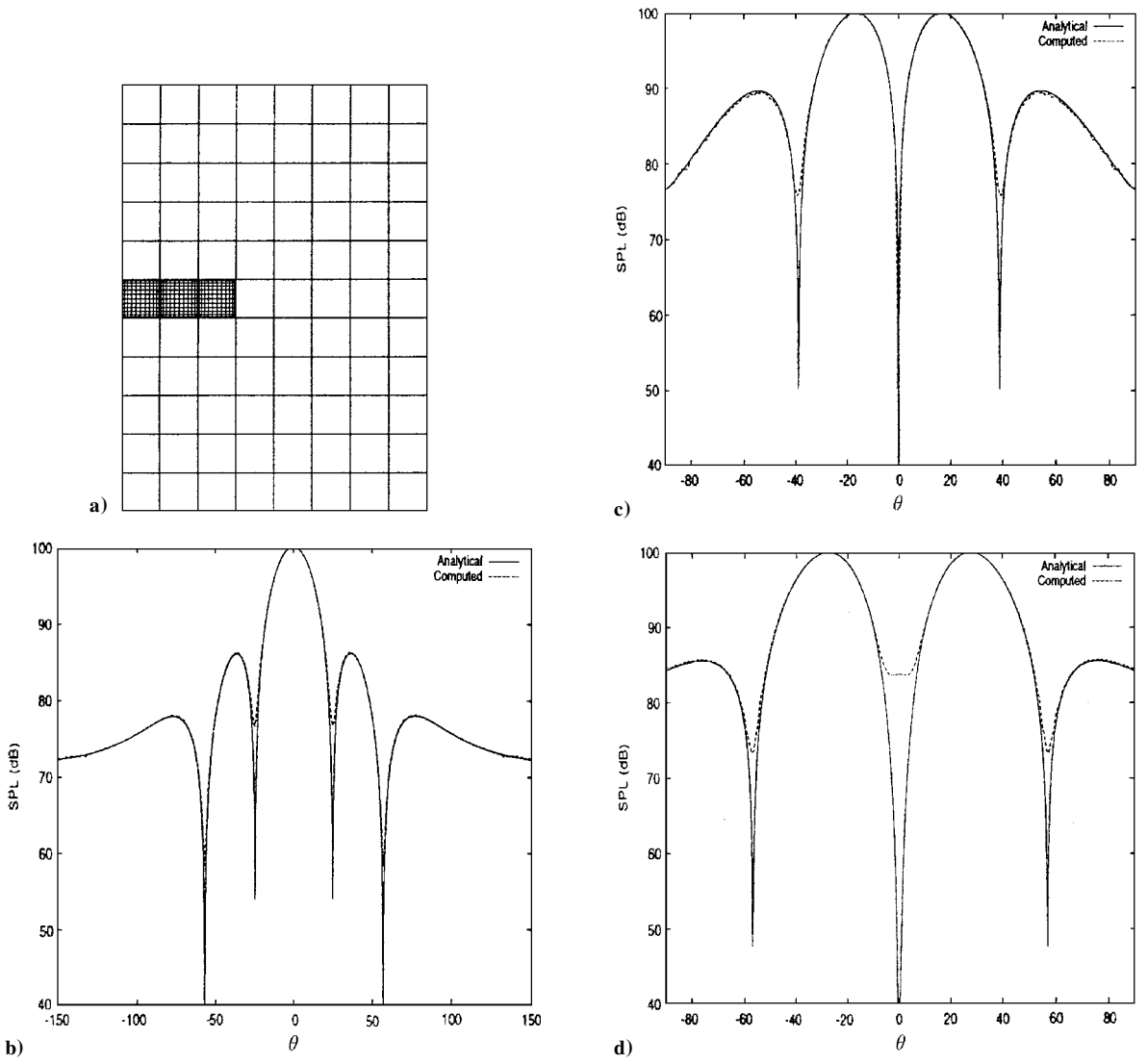

Fig. 1 Radiation from slab-symmetry flat duct: a) computational domain (grids shown in the domains inside the duct), b) plane wave directivity pattern, c) first cross mode, and d) second cross mode.

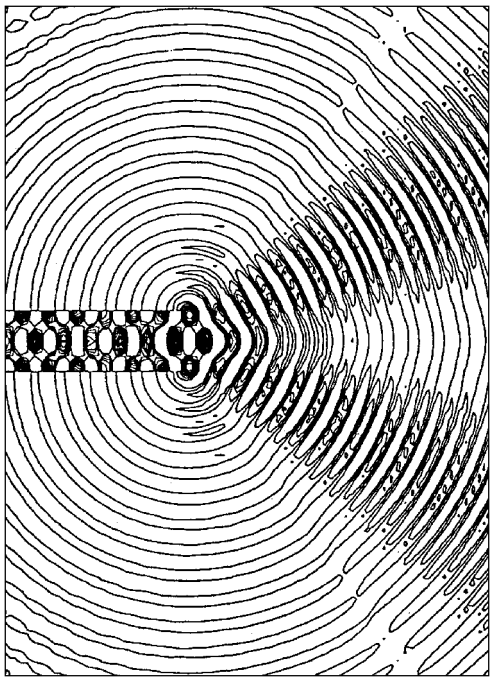

Fig. 2 Acoustic pressure contours for the slab-symmetry flat duct, second cross mode.

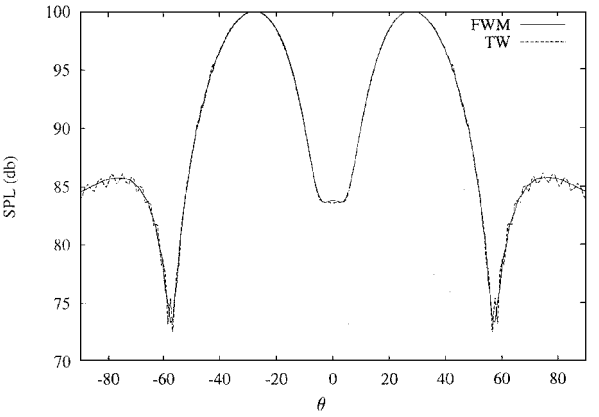

Fig. 3 Directivity for the second cross mode computed with the finite wave model (FWM) and the Tam and Webb[3] (TW) radiation boundary condition.

0.5 and no centerbody, under forward flight conditions with infinity Mach number $M = 0.21$. The reference length is the interior radius of the duct. The mesh is made up of 105 elements, with $N = 10$ Gauss points per element, and extends 10.5 radii from the fan face in the axial direction and 8 radii from the duct axis in the radial direction. The nonuniform flowfield surrounding the duct is obtained by driving the residuals to machine precision. The boundary condition used at the fan face for this steady-state computation is a specified

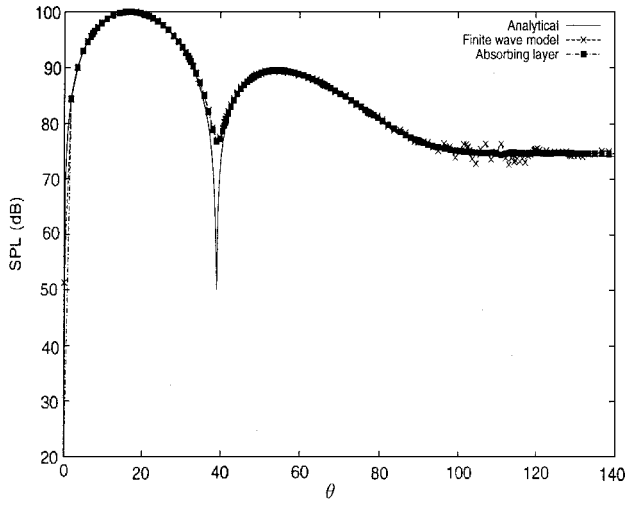

Fig. 4 Directivity pattern for the first cross mode computed with and without the damping layer; comparison to the analytical solution.

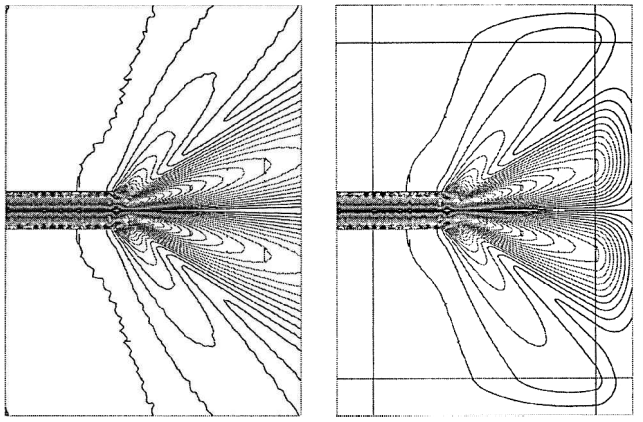

a) b)

Fig. 5 First cross mode rms pressure contours (30 contours between 2e-9 and 8-5) obtained using a) the finite wave model and b) the finite wave model plus an absorbing layer (shown) with $\sigma_M = 2.5$.

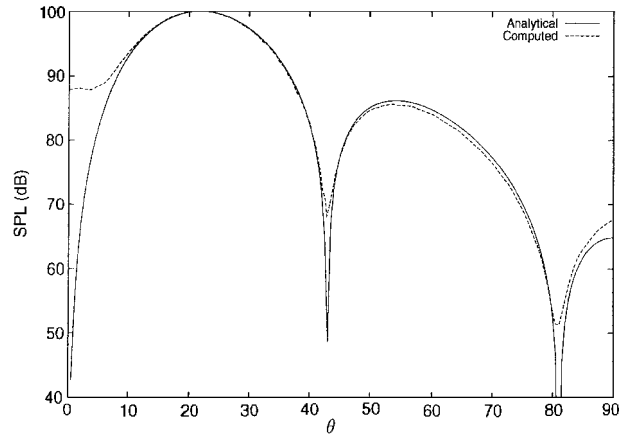

Fig. 6 Directivity pattern for axisymmetric flat duct radiation compared to the analytical solution for radiation from a circular piston vibrating in the same radial mode given by Tyler and Sofrin.[20]

pressure of $0.96p_\infty$. Thereafter, the acoustic source at the fan face is turned on, using a relatively large pressure amplitude of 1.4% of the fan face pressure. A damping region with a nondimensional depth of 1.3 in each direction and damping coefficients $\sigma_M = 90$ and $\beta = 6$ are used for the acoustic part of the computations. Unsteady computations are carried on up to $t = 45$, which is about three times the interval needed for an acoustic perturbation at the fan face to propagate out of the domain.

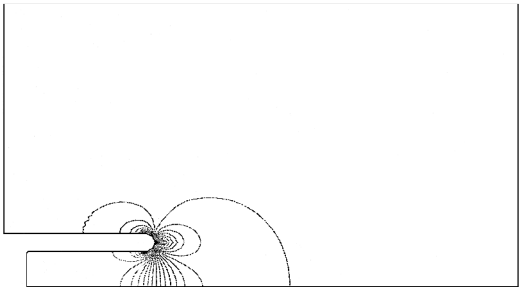

Fig. 7 Mean flow Mach contours for the bell-mouth duct in $M = 0.21$ forward flight (50 contours from 4.86e-3 to 4.53e-1).

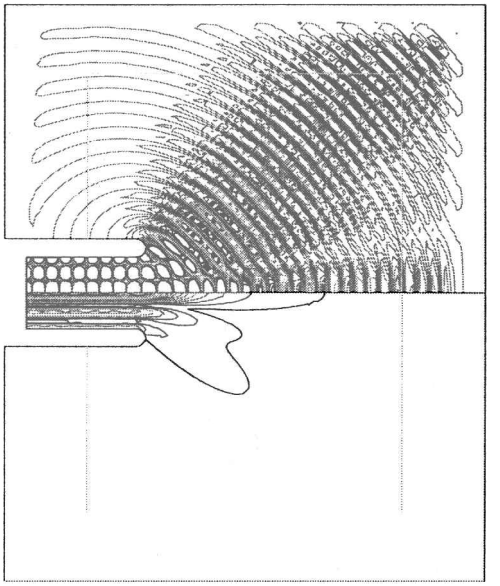

Fig. 8 Acoustic and rms pressure contours for the (0, 2) mode radiation in $M = 0.21$ flight from the bell-mouth duct.

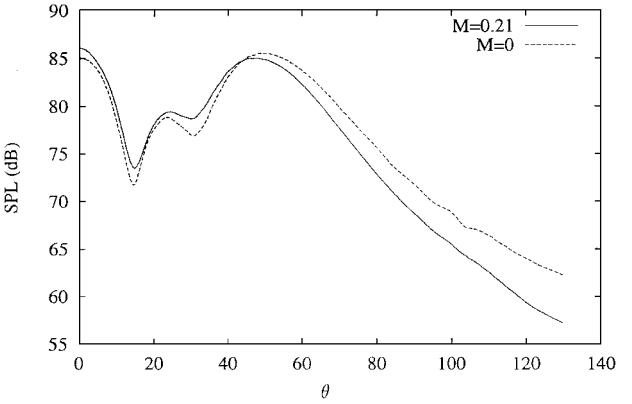

Fig. 9 Directivity pattern for the bell-mouth duct with and without flow, mode (0, 2).

Mach number contours of the computed mean flow are shown in Fig. 7. In the steady-state computations, the far-field boundary fluxes are obtained by solving a Riemann problem between the infinity state and the state extrapolated from inside the computational domain. Acoustic radiation of the second radial mode with axial symmetry, mode (0, 2), at a reduced frequency of 9.0 is computed. When mean flow effects are accounted for, there are about four mesh points per wavelength for the highest frequency expected to be present in the computation. Figure 8 shows the acoustic pressure and the rms pressure contours for the (0, 2) mode. The damping layer is highlighted in Fig. 8, such that one can notice the attenuation of the acoustic waves upon penetration in the layer.

Figure 9 shows the directivity pattern obtained on the interior boundary of the damping layer in the case with flow compared with

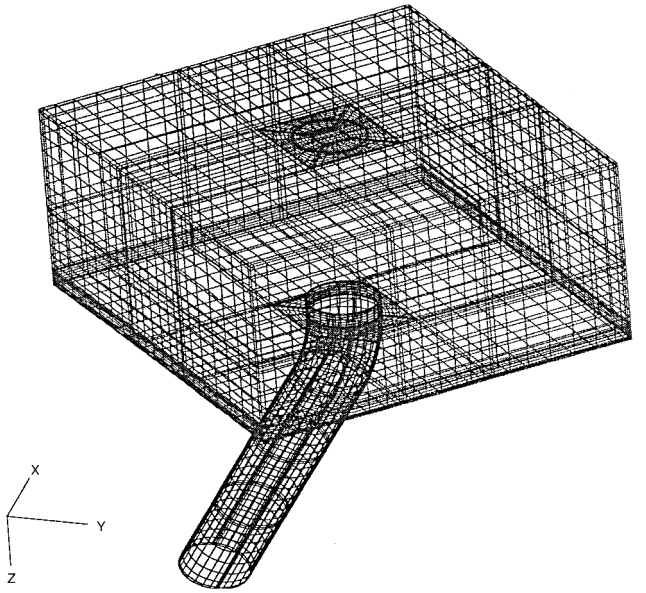

Fig. 10 Wire frame of the mesh used for the turboshaft inlet model.

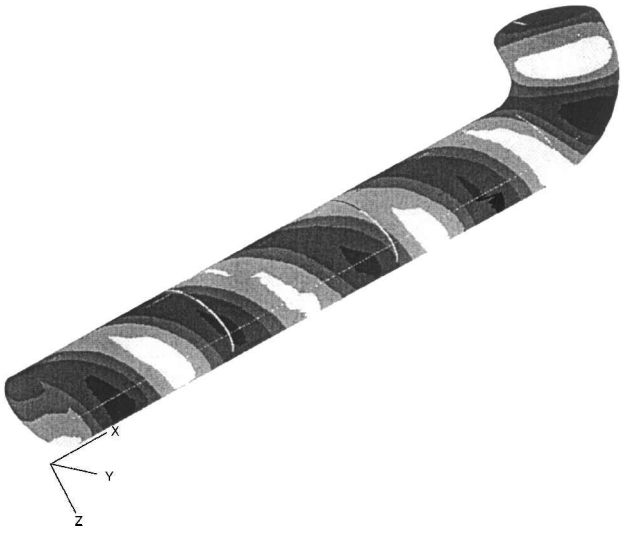

Fig. 11 Instance of acoustic pressure for the turboshaft inlet model, first azimuthal mode.

the no-mean-flow case ($M = 0$). Data are normalized in both cases so that the pressure amplitude at the fan face, which is the same for both computations, is at 100 dB. The major effect of the flow is to shift the position of the main lateral lobe by about 4 deg toward the axis, as expected. Also, there is an increase in acoustic radiation along the axis of the fan. Although the boundary is too close for the results to be considered as representative for the far field, they do give an indication about the actual trends. These results can ultimately be extended to large distances from the nacelle using a Kirchhoff surface technique.[1]

Generic Turboshaft Engine Inlet

Finally, results for the three-dimensional propagation of spinning modes inside a simplified model of a helicopter turboshaft engine inlet are presented. The curved duct used to this end is made up of three parts. Using the duct radius R_0 for nondimensionalization, the source plane is located at the beginning of a straight circular duct 11.76 units long. The axis of symmetry of this cylinder is taken as the x axis. The duct continues with a torus of internal radius 0.6 and external radius 2.6 and another straight duct 0.66 units long, from the exit plane of which sound is radiated into free space.

A frequency of 1000 Hz is considered, which corresponds to a nondimensional angular frequency $\omega R_0/c = 2.772$. Propagation of plane wave mode (0, 0) and the first azimuthal mode (1, 0) is analyzed. A typical mesh used for the computation is shown in

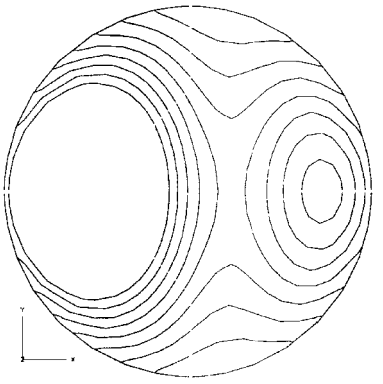

a) Plane wave

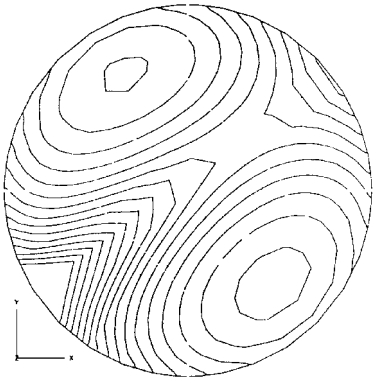

b) First azimuthal mode

Fig. 12 Duct exit plane rms pressure contours for the turboshaft engine inlet model.

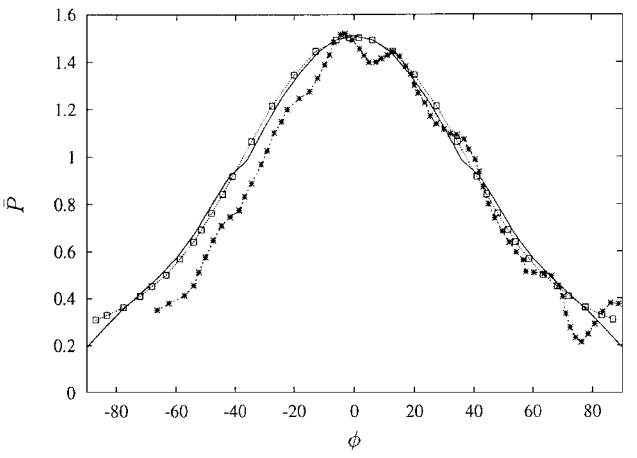

a) Plane wave

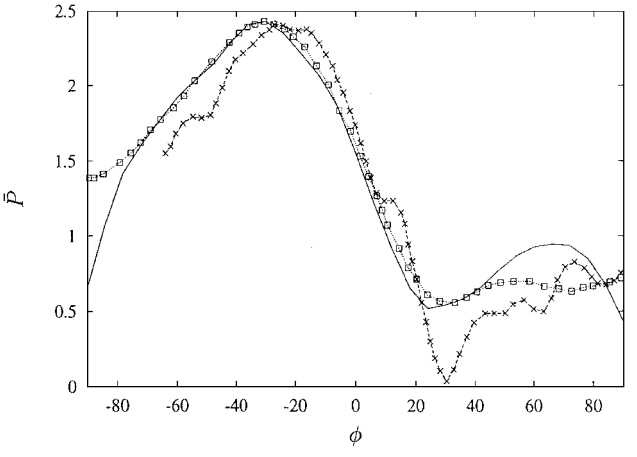

b) First azimuthal mode

Fig. 13 RMS pressure directivity in the x = 13.36 plane: ——, present solution; □, BIM computation[8]; ×, experiments.[8]

Fig. 10. It is made up of 71 elements, with 25 elements within the pipe. The number of points per wavelength was varied between five and six ($N = 9$ to $N = 11$) without any noticeable changes in the results. Figure 11 shows an instance of the acoustic pressure for the first azimuthal mode on the duct surface.

For this computation, characteristic boundary conditions have been used at radiation boundaries. The primary interest was in the rms pressure distribution in the duct exit plane, contour plots of which are presented in Fig. 12. For the plane wave case, the rms pressure field is symmetric with respect to the $y = 0$ plane (the plane of symmetry of the duct), and there are only slight variations in sound pressure level on the duct exit plane. For the first azimuthal mode, the symmetry no longer exists, and the variations in rms pressure on the duct exit plane are much larger. The directivities in the $x = 13.36$ plane (passing through the center of the disk at the duct exit), computed on a sphere with radius $5R_0$, are shown in Fig. 13. As can be seen, they compare very well with both the boundary integral method (BIM) computation and the experiments by Malbéqui et al.[8]

The operation count is asymptotically proportional to N^4 in three dimensions and varies linearly with the number of elements. For instance, the present grid with $N = 11$ Gauss points required 64.5 μs per time step per grid point on the same R10000 processor as described earlier when a five-stage Runge–Kutta scheme was used.

Conclusions and Future Work

A multidomain spectral method for the two-dimensional, axisymmetric and three-dimensional, nonlinear, time-dependent Euler equations supplemented by nonreflecting boundary conditions and modeling of duct acoustic modes has been developed. The overall methodology has been applied to the computation of sound fields generated by fans enclosed in rigid-wall ducts. Comparison of computed radiation patterns with analytical solutions for flat ducts showed very good agreement. It has also been demonstrated that the boundary conditions perform well for nonuniform mean flow cases. Based on these results, it is the authors' belief that multidomain spectral methods represent a viable alternative for aeroacoustic computations, especially in three dimensions when the number of grid points required by other methods is excessively large. Techniques for increasing the allowable time step, implementing a nonreflecting boundary condition at the source plane, speeding up convergence for steady-state computations, and treating possible flow discontinuities constitute the object of further research.

Acknowledgments

The support received from the Natural Sciences and Engineering Research Council of Canada and the Fonds pour la Formation de Chercheurs et l'Aide à la Recherche du Quebec is gratefully acknowledged. The first author wants to thank D. A. Kopriva and W. S. Don for several helpful discussions.

References

[1]Özyörük, Y., and Long, L. N., "Computation of Sound Radiating from Engine Inlets," *AIAA Journal*, Vol. 34, No. 5, 1996, pp. 894–901.

[2]Özyörük, Y., and Long, L. N., "A New Efficient Algorithm for Computational Aeroacoustics on Parallel Processors," *Journal of Computational Physics*, Vol. 125, No. 1, 1996, pp. 135–149.

[3]Tam, C. K. W., and Webb, J. C., "Dispersion-Relation-Preserving Finite Difference Schemes for Computational Acoustics," *Journal of Computational Physics*, Vol. 107, No. 2, 1993, pp. 262–281.

[4]Fornberg, B., *A Practical Guide to Pseudospectral Methods*, Cambridge Univ. Press, Cambridge, England, UK, 1996.

[5]Patera, A. T., "A Spectral Element Method for Fluid Dynamics: Laminar Flow in a Channel Expansion," *Journal of Computational Physics*, Vol. 54, No. 3, 1984, pp. 468–488.

[6]Hesthaven, J. S., "A Stable Penalty Method for the Compressible Navier–Stokes Equations. III. Multi Dimensional Domain Decomposition Schemes," *SIAM Journal on Scientific Computing*, Vol. 20, No. 1, 1999, pp. 62–93.

[7]Kopriva, D. A., and Kolias, J. H., "A Conservative Staggered-Grid Chebyshev Multidomain Method for Compressible Flows," *Journal of Computational Physics*, Vol. 125, No. 1, 1996, pp. 244–261.

[8]Malbéqui, P., Glandier, C., and Reynier, C., "Sound Propagation and Radiation in a Curved Duct," *AIAA Journal*, Vol. 34, No. 9, 1996, pp. 1778–1784.

[9]Hu, F. Q., Hussaini, M. Y., and Manthey, J., "Low-Dissipation and Low-Dispersion Runge–Kutta Schemes for Computational Acoustics," *Journal of Computational Physics*, Vol. 124, No. 1, 1996, pp. 177–191.

[10]Stanescu, D., and Habashi, W. G., "2N-Storage Low Dissipation and Dispersion Runge–Kutta Schemes for Computational Acoustics," *Journal of Computational Physics*, Vol. 143, No. 2, 1998, pp. 674–681.

[11]Carpenter, M. H., and Kennedy, C. A., "A Fourth-Order 2N-Storage Runge–Kutta Scheme," NASA TM-109112, June 1994.

[12]Hirsch, C., *Numerical Computation of Internal and External Flows*, Vol. 2, Wiley, New York, 1990, Chap. 19.

[13]Atkins, H., and Casper, J., "Nonreflective Boundary Conditions for High-Order Methods," *AIAA Journal*, Vol. 32, No. 3, 1994, pp. 512–518.

[14]Hu, F. Q., "On Absorbing Boundary Conditions for Linearized Euler Equations by a Perfectly Matched Layer," *Journal of Computational Physics*, Vol. 129, No. 1, 1996, pp. 201–219.

[15]Freund, J. B., "Proposed Inflow/Outflow Boundary Condition for Direct Computation of Aerodynamic Sound," *AIAA Journal*, Vol. 35, No. 4, 1997, pp. 740–742.

[16]Roe, P. L., "Approximate Riemann Solvers, Parameter Vectors, and Difference Schemes," *Journal of Computational Physics*, Vol. 43, No. 2, 1981, pp. 357–372.

[17]Dong, T. Z., Shih, S. H., Mankbadi, R. R., and Povinelli, L. A., "A Numerical Study of Duct Geometry Effect on Radiation of Engine Internal Noise," AIAA Paper 97-1604, May 1997.

[18]Mani, R., "Refraction of Acoustic Duct Waveguide Modes by Exhaust Jets," *Quarterly of Applied Mathematics*, Vol. 30, Jan. 1973, pp. 501–520.

[19]Savkar, S. D., "Radiation of Cylindrical Duct Acoustic Modes with Flow Mismatch," *Journal of Sound and Vibration*, Vol. 42, No. 3, 1975, pp. 363–386.

[20]Tyler, J. M., and Sofrin, T. G., "Axial Flow Compressor Noise Studies," *SAE Transactions*, Vol. 70, 1962, pp. 309–332.

P. J. Morris
Associate Editor